Summer 8-2023

Design of Microwave Superconducting Resonators for Materials Characterization

Xinyi Zhao

WASHINGTON UNIVERSITY IN ST. LOUIS

McKelvey School of Engineering
Department of Electrical & Systems Engineering

Thesis Examination Committee:
Kater Murch, Chair
Shantanu Chakrabartty
Chuan Wang

Design of Microwave Superconducting Resonators for Materials Characterization

by
Xinyi Zhao

A thesis presented to
the McKelvey School of Engineering
of Washington University in
partial fulfillment of the
requirements for the degree
of Master of Science

August 2023
St. Louis, Missouri

Table of Contents

List of Figures . . . . . **iii**

List of Tables . . . . . **v**

Acknowledgments . . . . . **vi**

Abstract . . . . . **viii**

Chapter 1: Introduction **1**

Chapter 2: Theory **2**
2.1 Transmission line 2
2.2 Microwave resonator 7
2.3 Transmission line resonator 11
2.4 Coplanar waveguide (CPW) resonator 12
2.5 Coupled coplanar waveguide resonator 13
2.6 Differential & common modes 14
2.7 Coupling 15
2.8 S-parameters 16

Chapter 3: Design & simulation **18**
3.1 Goals 18
3.2 Design 20
3.3 Simulation 22

Chapter 4: Other applications **28**
4.1 Fabrication issue detection 28
4.2 Resonator frequency tuning 32

Chapter 5: Conclusion **36**

References **37**

List of Figures

Figure 2.1: A transmission line with corresponding voltage and current. 3

Figure 2.2: A piece of unit length transmission line's equivalent circuit with lumped element. 3

Figure 2.3: The wave functions with the boundary condition. 5

Figure 2.4: A transmission line connected to a load impedance Z_L. 6

Figure 2.5: A modeled resonator by series RLC circuit. 8

Figure 2.6: Magnitude of input impedance versus frequency. 8

Figure 2.7: A modeled resonator by parallel RLC circuit. 10

Figure 2.8: Magnitude of input impedance versus frequency. 10

Figure 2.9: The wavelength for the transmission line resonator with different ends. . 12

Figure 2.10: CPW resonator 12

Figure 2.11: CCPW resonator. 13

Figure 2.12: CCPW resonator cross-section. 14

Figure 2.13: A two-port network. 16

Figure 2.14: S-parameters plots. 17

Figure 3.1: A quarter-wavelength resonator coupled to a transmission line. 18

Figure 3.2: The circuit diagram of a resonator coupled to a transmission line. 19

Figure 3.3: Ideal S-parameter results. 20

Figure 3.4: The different cuts on a quartz substrate. 21
Figure 3.5: The complete chip design with a quartz substrate. 22
Figure 3.6: The eigenmode simulations. 24
Figure 3.7: The HFSS simulation E-field and mesh plots. 26
Figure 3.8: The HFSS simulation S-parameter results. 27
Figure 3.9: The cross-section of a CPW resonator. 27

Figure 4.1: The ideally etched CCPW resonator. 29
Figure 4.2: The over-etched CCPW resonator. 29
Figure 4.3: The resonator frequency v.s. Trench depth. 29
Figure 4.4: The experimental setup 30
Figure 4.5: The neon deposition on a resonator. 31
Figure 4.6: The frequency shift v.s. the neon thickness change. 31
Figure 4.7: The equivalent discrete circuit for an ideal third-order low-pass filter. . . 33
Figure 4.8: The equivalent discrete circuit for an integrated filter. 34
Figure 4.9: The entire design with resonator and filters. 35

List of Tables

Table 3.1: The transmission lines' and resonators' widths. 21

Table 4.1: The ideal inductance and capacitance for a third-order Butterworth filter. 33

Acknowledgments

I would like to express my sincere gratitude to my thesis advisor, Professor Kater Murch, for his invaluable guidance and support throughout my thesis project. I am also grateful to professor David Wisbey who have provided me with feedback and insights that have helped me improve my research.

I would like to express my heartfelt appreciation to all the members in Murch research group, whose unwavering support and inspiration have been integral to my academic journey. First and foremost, I would like to thank Kaiwen Zheng, who has been my mentor and guide, and has helped me with all my projects. Without his support, I would not have been able to pursue my research interests and secure a place in a prestigious PhD program. I am also grateful to Chandrashekhar Gaikwad and Daria Kowsari, who have been an invaluable source of research knowledge, providing me with training, guidance, and feedback throughout my project.

I would like to extend my thanks to Yunzhao Wang, Xingrui Song, Weijian Chen, Serra Erdamar, Xiayu Linpeng, Maryam Abbasi, and Alexandria Udenkwo as well, who have provided me with emotional support, encouragement, and positivity during the challenging times of my research. Their insights and feedback have helped me grow both personally and academically, and I am truly grateful for their contributions.

I am also grateful to my parents for their unconditional love and support, for always believing in me, and for providing me with the financial means to pursue my studies. Their unwavering support has been the foundation of my success and has given me the strength to overcome any obstacle.

I am deeply indebted to my friends, whose unwavering emotional support and encouragement have sustained me throughout my academic journey. Their kind words and gestures of support have lifted my spirits and kept me motivated, and I cannot thank them enough for their friendship.

Moreover, I would like to thank YouTube and Bilibili for their vast resources on different electronic software. These platforms have been a valuable resource in helping me understand and master various software tools, and I am grateful for their contribution to my learning.

I would like to express my sincere appreciation to all the plants that I purchased and cared for in our lab, even though they ultimately met an untimely demise. Despite their short-lived presence, their beauty and serene presence brought a sense of tranquility to our lab space. I acknowledge the significant role they played in enhancing my life, and I am truly appreciative of the happiness they brought to me and my fellow lab mates.

Finally, I would like to thank all those who have made this thesis possible. Your contributions and support have been invaluable.

Xinyi Zhao

Washington University in St. Louis
August 2023

ABSTRACT OF THE THESIS

Design of Microwave Superconducting Resonators for Materials Characterization

by

Xinyi Zhao

Master of Science in Electrical Engineering

Washington University in St. Louis, 2023

Professor Kater Murch, Chair

This thesis focuses on designing microwave superconducting resonators for materials characterization. Three projects were conducted to achieve this goal:

Firstly, coplanar waveguide (CPW) resonators were designed to measure the loss of quartz. These resonators were designed and characterized using engineering software, which showed that the CPW resonator is a sensitive tool for measuring the loss of quartz.

Secondly, a novel approach was developed for detecting fabrication issues in coupled coplanar waveguide (CCPW) resonators. The method is based on the changes in the resonance frequency of the CCPW resonator due to problems arising in the fabrication process. This approach was demonstrated by fabricating CCPW resonators with intentionally introduced defects and measuring their resonance frequencies. The results showed that the method effectively detects fabrication issues and can potentially improve the fabrication process from dry etch to wet etch.

Lastly, a DC source's effect on a CPW resonator's resonance frequency was studied. The results showed that the resonance frequency of the CPW resonator could be tuned by applying a DC source to it. This technique has potential applications in developing tunable filters and sensors.

Overall, the work presented in this thesis demonstrates the usefulness of superconducting resonators in materials characterization and highlights their potential for use in various microwave engineering applications. These projects provide novel insights into the design and performance of superconducting resonators and open up promising avenues for future research in this area.

Chapter 1

Introduction

Microwave superconducting resonators have proven to be an invaluable tool for materials characterization, owing to their exceptional attributes such as high sensitivity, minimal loss, and extensive frequency range. The primary objective of this thesis is to delve into the intricate aspects of microwave superconducting resonator design, simulation, and their significant applications within the field of quantum science.

The thesis is divided into three parts. The first part provides an overview of the theory behind microwave resonators, including transmission line theory, different types of resonators, different resonator modes, coupling, and S-parameters. This foundation sets the stage for the design and simulation of resonators, which is the focus of the second part of the thesis.

In this part, we use the design of resonators on quartz as an example to explain the step-by-step process of designing and simulating microwave superconducting resonators. The quartz project serves as a practical demonstration of the design principles covered in the first part of the thesis.

Finally, the third part of the thesis explores the applications of microwave superconducting resonators beyond materials characterization. Specifically, we investigate using changes in resonator frequency to detect fabrication issues and apply DC sources to tune the resonator frequency. Overall, this thesis aims to comprehensively understand microwave superconducting resonators and their applications in materials characterization and beyond.

Chapter 2

Theory

2.1 Transmission line

Radio waves can propagate in two distinct ways: through unbounded media, such as in the case of radio broadcasting, and by using guided structures, like waveguides. One of the most common types of a waveguide is the transmission line, specifically designed to transmit electrical power or signals from one point to another. Typically depicted with two lines in a schematic diagram, as shown in Figure 2.1, a transmission line always consists of at least two conductors.

To analyze a transmission line, it's often necessary to simplify it into a discrete circuit. When two pieces of metal are placed near each other, positive and negative charges can accumulate, creating an electric field that stores energy. Similarly, a wire-carrying current creates a magnetic field that also stores energy. These energies are the sources of capacitive and inductive effects that affect the behavior of a transmission line. Therefore, a transmission line can be modeled as an LC circuit, as shown in Figure 2.2.[1] The impedance in the waveguide determines the other two elements in the circuit.

The lumped-element circuit model for the transmission line is illustrated in Figure 2.1. we can represent it as a series of smaller segments with a unit length of Δz and then model each component as a circuit element in Figure 2.2. The previously mentioned variables can be defined as follows:

R = series resistance per unit length, for both conductors, in Ω/m

L = series inductance per unit length, for both conductors, in H/m

G = shunt conductance per unit length, in S/m

C = shunt capacitance per unit length, in F/m

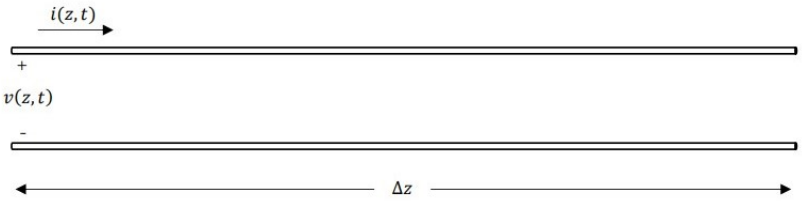

Figure 2.1: A transmission line with corresponding voltage and current.

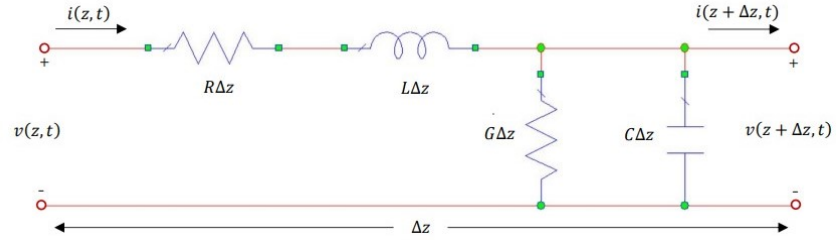

Figure 2.2: A piece of unit length transmission line's equivalent circuit with lumped element.

The circuit elements L and C in the equivalent model for a transmission line are a result of self-inductance and capacitance between the two conductors. The element R arises from the finite conductivity of the conductors, while the element G accounts for dielectric loss between them.

By applying Kirchoff's voltage and current laws to the circuit in Figure 2.2, we have,

$$v(z,t) - R\Delta z i(z,t) - L\Delta z \frac{\partial i(z,t)}{\partial t} - v(z+\Delta z,t) = 0, \tag{2.1}$$

$$i(z,t) - G\Delta z v(z+\Delta z,t) - C\Delta z \frac{\partial v(z+\Delta z,t)}{\partial t} - i(z+\Delta z,t) = 0. \tag{2.2}$$

We simplify (2.1) and (2.2) by taking $\Delta z \to 0$,

$$\frac{\partial v(z,t)}{\partial z} = -Ri(z,t) - L\frac{\partial i(z,t)}{\partial t}, \tag{2.3}$$

$$\frac{\partial i(z,t)}{\partial z} = -Gv(z,t) - C\frac{\partial v(z,t)}{\partial t}. \tag{2.4}$$

When performing them to be made by superconductor under a lossless environment, there is no contribution to loss from the circuit elements R or G. Therefore, we set $R = G = 0$, and use this simplification to convert the first-order equations (2.3) and (2.4) into second-order equations.[2]

$$\frac{\partial^2 V}{\partial z^2} - LC\frac{\partial^2 V}{\partial t^2} = 0, \tag{2.5}$$

$$\frac{\partial^2 I}{\partial z^2} - LC\frac{\partial^2 I}{\partial t^2} = 0. \tag{2.6}$$

By solving the equations, we have,

$$V = V_0^+ e^{-\gamma z} + V_0^- e^{\gamma z}, \tag{2.7}$$

$$I = I_0^+ e^{-\gamma z} + I_0^- e^{\gamma z}, \tag{2.8}$$

where the propagation constant is,

$$\gamma = j\omega\sqrt{LC}. \tag{2.9}$$

Consequently, the characteristic impedance of the transmission line is

$$Z_0 = \frac{V}{I} = \sqrt{\frac{L}{C}}. \tag{2.10}$$

Transmission line theory models the transmission of signals between devices, considering the transmission line's characteristic impedance. When a signal is transmitted from a device with impedance Z_0 into a receiving device with impedance Z_L, a portion of the signal is reflected toward the source due to the impedance mismatch, resulting in signal loss.[3]

In electrical engineering, when two devices are connected through a transmission line, the signal transfer efficiency can be maximized by minimizing loss due to impedance mismatch.

Assuming the input signal is a traveling wave, it can be represented as a right-moving traveling wave with a specific wave function before reaching the boundary between Z_0 and Z_L.[4]

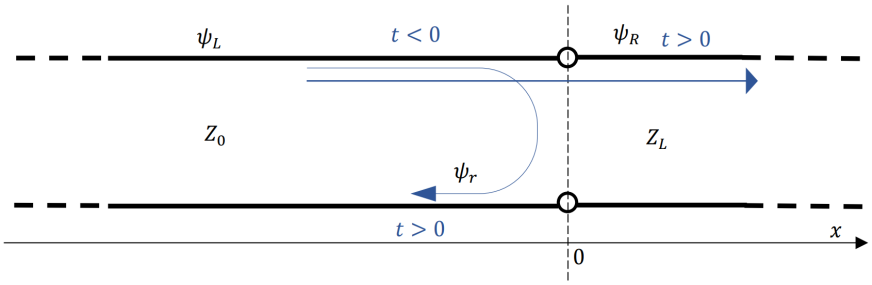

Figure 2.3: The wave functions with the boundary condition.

$$\psi_L(x,t) = \psi_i(x - v_1 t), \quad t < 0. \tag{2.11}$$

The function $\psi_L(x,t)$ is a component of the traveling wave $\psi(x,t)$, which is defined for $x < 0$. The shape of the wave in this region is described by the function $\psi_i(x)$. After $t = 0$, ψ_L consists of both left and right-moving components, which means it can be expressed as a superposition of these two components.

$$\psi_L(x,t) = \psi_i(t - \frac{x}{v_1}) + \psi_r(t + \frac{x}{v_1}). \tag{2.12}$$

Here, ψ_r is the reflected wave and the presence of a reflected wave is not necessary for ψ_L to exist. However, it is possible to express any wave as a sum of left-moving and right-moving components.

Beyond $t = 0$, a transmitted wave is present and exclusively moves towards the right,

$$\psi_R(x,t) = \psi_t(t - \frac{x}{v_2}). \tag{2.13}$$

Now, we apply the boundary condition at $x = 0$, where signals transfer from Z_0 to Z_L.

$$\psi_i(t) + \psi_r(t) = \psi_t(t). \tag{2.14}$$

The equation can be solved as

$$\psi_r = \frac{\frac{T_1}{v_1} - \frac{T_2}{v_2}}{\frac{T_1}{v_1} + \frac{T_2}{v_2}}\psi_i. \tag{2.15}$$

Impedance is defined as the ratio of tension to velocity, represented by $Z_0 = \frac{T_1}{v_1}$ and $Z_L = \frac{T_2}{v_2}$ for the two media involved. The degree of mismatch between impedances determines the amount of wave reflection that occurs. Mismatching always occurs unless the impedances of the two media are identical.

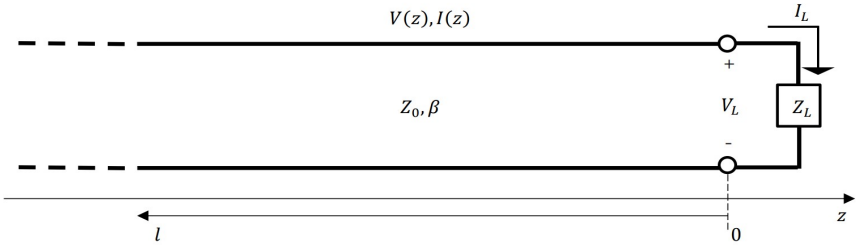

Figure 2.4: A transmission line connected to a load impedance Z_L.

Figure 2.4 displays a transmission line connected in series with an impedance load, denoted as Z_0 and Z_L, respectively. In the case that Z_0 and Z_L are not equal, power is partially transmitted while the remaining portion is reflected, resulting in energy loss.[3] Therefore, it is important to design all circuit elements to have an impedance of 50 Ω, which is the same as the impedance of the objects used in experiments.

To analyze the reflection phenomenon, the amplitudes of the transmitted and reflected signals need to be considered. Equation (2.8) provides the expression for the current in this scenario.

$$I = \frac{V}{Z_0} = \frac{V_0^+}{Z_0}e^{-\gamma z} - \frac{V_0^-}{Z_0}e^{\gamma z}. \tag{2.16}$$

The total voltage and current at the load are solely determined by the load impedance in Figure 2.4. Therefore, the voltage and current values obtained at $z = 0$ are the parameters for measuring the load's behavior.

$$Z_L = \frac{V(z=0)}{I(z=0)} = \frac{V_0^+ + V_0^-}{V_0^+ - V_0^-} Z_0. \tag{2.17}$$

And the relationship between the amplitudes is,

$$V_0^- = \frac{Z_L - Z_0}{Z_L + Z_0} V_0^+. \tag{2.18}$$

So, the voltage reflection coefficient, Γ, is defined as,

$$\Gamma = \frac{V_0^-}{V_0^+} = \frac{Z_L - Z_0}{Z_L + Z_0}. \tag{2.19}$$

2.2 Microwave resonator

A microwave resonator is an electronic device that stores and manipulates microwave electromagnetic energy. It is composed of a closed cavity or structure designed to resonate at a particular frequency. When an electromagnetic wave with this frequency is introduced into the resonator, it generates a standing wave pattern within the cavity. The standing wave, in turn, causes the energy to become trapped and stored within the resonator.[1]

Resonators are commonly represented using RLC circuits, which demonstrate resonance at a specific frequency. The lumped elements in these circuits can be arranged in either a series or parallel configuration. Figure 2.5 displays the equivalent circuit for the series configuration. In this case, the input impedance can be expressed as:

$$Z_{in} = R + j\omega L - j\frac{1}{\omega C}. \tag{2.20}$$

The power dissipated by the resistor R is,

$$P_{loss} = \frac{1}{2}|I|^2 R. \tag{2.21}$$

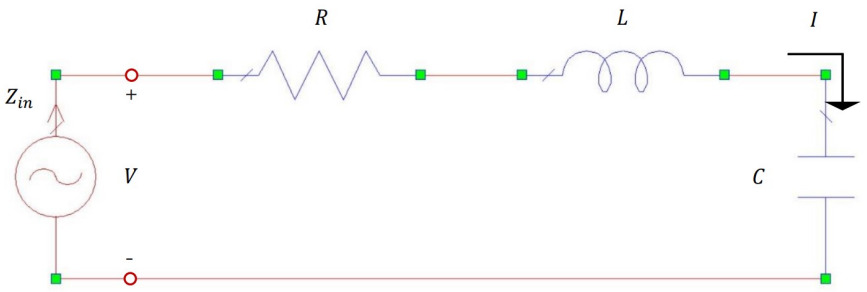

Figure 2.5: A modeled resonator by series RLC circuit.

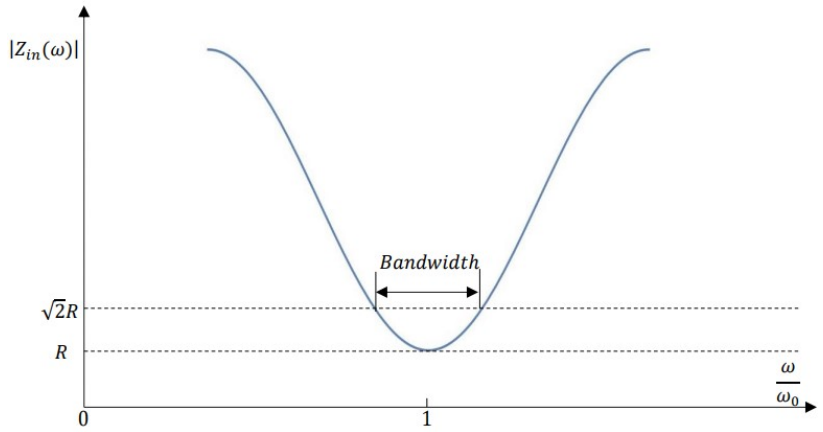

Figure 2.6: Magnitude of input impedance versus frequency.

The average magnetic energy stored in the inductor L is,

$$W_m = \frac{1}{4}|I|^2 L. \tag{2.22}$$

And the average electric energy stored in the capacitor C is,

$$W_e = \frac{1}{4}|V_c|^2 C = \frac{1}{4}|I|^2 \frac{1}{\omega^2 C}. \tag{2.23}$$

V_c refers to the voltage that exists across the capacitor. Resonance in a circuit occurs when the average magnetic energy is equal to the average electric energy, resulting in the input impedance being equal to R. By using equations (2.22) and (2.23), the resonance frequency can be calculated:

$$\omega_0 = \frac{1}{\sqrt{LC}}. \tag{2.24}$$

The resonator quality factor, or Q_r, is a crucial parameter for circuits. It represents the ratio of energy stored in an oscillating resonator to the energy dissipated per cycle by damping processes.[5] In other words, it quantifies the efficiency of a resonator by comparing how much energy is stored in it versus how much is lost during each oscillation cycle. A high Q_r value indicates a more efficient resonator, meaning it can sustain oscillations without significant energy loss for longer periods. Therefore, Q_r is a critical parameter that influences the performance and stability of circuits, and it is essential to consider when designing or analyzing resonator-based systems.

$$Q = \frac{W_m + W_e}{P_{loss}}\omega. \tag{2.25}$$

By definition,

$$Q = \frac{energy\ stores}{power\ loss}\omega. \tag{2.26}$$

The quality factor can also be calculated by,

$$Q = \frac{resonance\ frequency}{\Delta f_{-3dB}}. \tag{2.27}$$

Δf_{-3dB} is the full width half max linewidth bandwidth.

At resonance, by applying (2.21), (2.22), and (2.23),

$$Q_r = \frac{1}{\omega_0 RC}. \tag{2.28}$$

The parallel RLC circuit is connected as in Figure 2.7. The input impedance becomes

$$Z_{in} = (\frac{1}{R} + \frac{1}{j\omega L} + j\omega C)^{-1}. \tag{2.29}$$

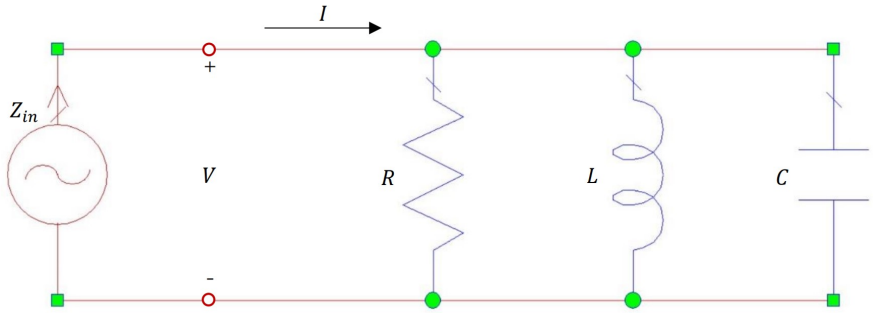

Figure 2.7: A modeled resonator by parallel RLC circuit.

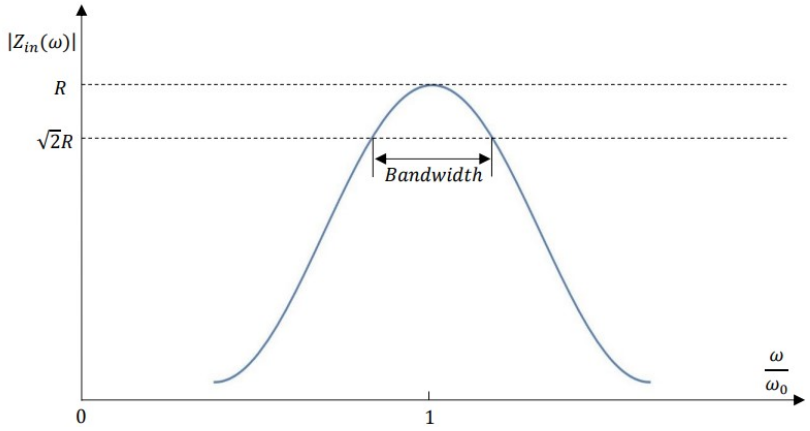

Figure 2.8: Magnitude of input impedance versus frequency.

The power dissipated by resistor R, the average electric energy stored in capacitor C, and the average magnetic energy stored in inductor L are,

$$P_{loss} = \frac{|V|^2}{2R}, \tag{2.30}$$

$$W_m = \frac{1}{4}|I_L|^2 L = \frac{1}{4}\frac{|V|^2}{\omega^2 L}, \tag{2.31}$$

$$W_e = \frac{1}{4}|V|^2 C. \tag{2.32}$$

Similarly, the resonance frequency and resonator quality factor can be included as,

$$\omega_0 = \frac{1}{\sqrt{LC}}, \tag{2.33}$$

$$Q_r = \omega_0 RC. \tag{2.34}$$

Q_r characterizes the quality factor of a resonator when it is unloaded, meaning no external conditions affect its performance. However, when a resonator is loaded by external factors, such as a circuit or other components, an external quality factor, Q_e, comes into play. The total quality factor Q can then be calculated as the inverse sum of Q_r and Q_e.[6]

$$\frac{1}{Q} = \frac{1}{Q_r} + \frac{1}{Q_e}. \tag{2.35}$$

This equation describes how the external factors affect the overall efficiency of the resonator, and it is crucial to consider both Q_r and Q_e when designing or analyzing resonator-based systems.

2.3 Transmission line resonator

Transmission lines can be modeled using an equivalent circuit diagram similar to that of a resonator. Therefore, a transmission line of a certain length can be considered a transmission line resonator. The two ends of a resonator can either be open (open to the ground) or shorted (connected to the ground), which results in two types of resonators: $\frac{\lambda}{2}$ (half-wavelength) and $\frac{\lambda}{4}$ (quarter-wavelength) resonators.

A transmission line resonator with both ends open or short has a physical length of $\frac{\lambda}{2}n$, for $n \in \mathbb{N}$. On the other hand, a resonator with one end open and the other short has a length of $\frac{\lambda}{4}n$. When both ends are shorted, the resonator is equivalent to the series RLC circuit depicted in Figure 2.5. Conversely, the resonators with one end open and the other shorted are equivalent to the parallel RLC circuit shown in Figure 2.7.

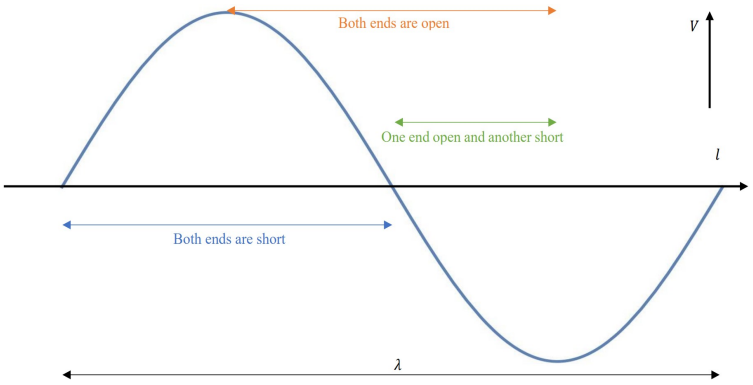

Figure 2.9: The wavelength for the transmission line resonator with different ends.

2.4 Coplanar waveguide (CPW) resonator

A CPW resonator is a type of planar transmission line resonator designed to support standing waves at a specific frequency. The CPW resonator is composed of conductors that are placed above the substrate, with one conductor serving as the center pin located between the other conductors. Figure 2.10 shows the open and shorted half-wavelength CPW resonators.

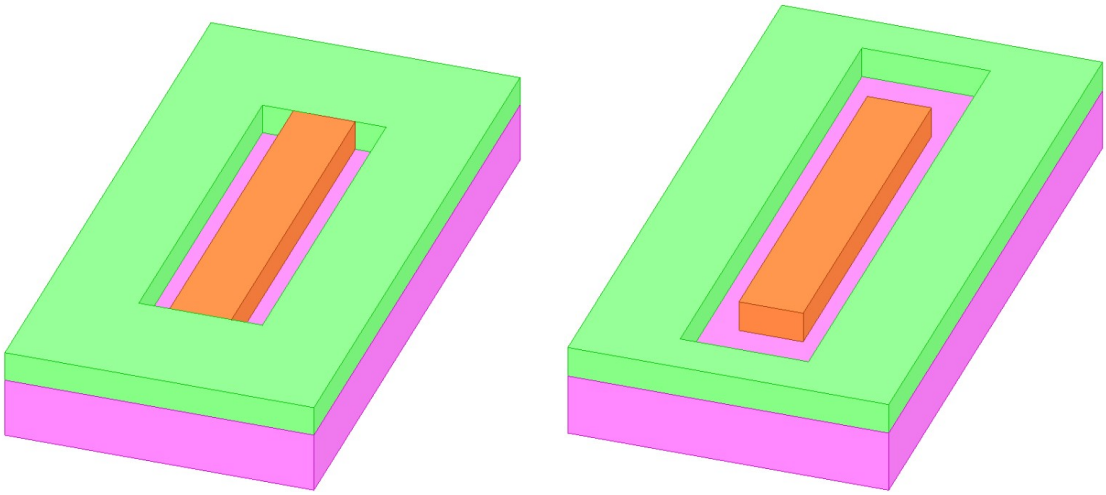

Figure 2.10: CPW resonators. The purple block is the substrate. The green and orange bulks are the conductors, and the orange one is the center pin. Left: Half-wavelength CPW resonator with both ends shorted. Right: Half-wavelength CPW resonator with both ends open.

In the CPW resonator, the conductor acts as an inductor when current flows through it, while each pair of conductors acts as a capacitor. This structure forms an RLC circuit,

with the resonance frequency determined by the conductors' size. Therefore, modifying the size of the conductors can alter the resonance frequency.[7]

2.5 Coupled coplanar waveguide resonator

Coupled coplanar waveguide (CCPW) resonator consists of two conductor strips placed between two ground planes, all on the same plane. The conductor strip is usually shaped into a meander or spiral pattern to increase the circuit's inductance, while the gap between the strip and the ground planes functions as a capacitor, as depicted in Figure 2.11.[8] When excited by an electromagnetic wave, the CCPW resonator produces a resonance at a specific frequency. CCPW resonators are preferred over other resonant circuits because of their low loss, small size, and compatibility with integrated circuit technologies.

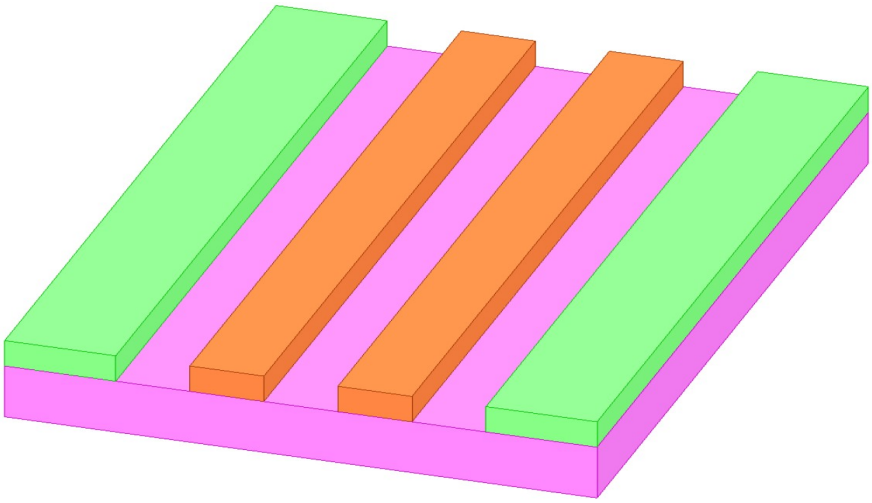

Figure 2.11: Side view of CCPW resonator. The purple block is the substrate. The green and orange bulks are the conductors, and the orange bulks are the strips.

Since the resonator has two strips, the same or opposite voltages can be applied to the strips resulting in common and differential modes.

2.6 Differential & common modes

A resonator can operate in two different modes depending on the input signal applied to it: differential mode and common mode.

Let's consider the CCPW resonator as an example. As shown in Figure 2.12, the resonator's structure can be represented as an LC circuit.[9] Using this representation, we can write the inductance and capacitance matrices as follows:

$$L = \begin{pmatrix} L_{11} & L_{12} \\ L_{21} & L_{22} \end{pmatrix}, \tag{2.36}$$

$$C = \begin{pmatrix} C_{11} & C_{12} \\ C_{21} & C_{22} \end{pmatrix}. \tag{2.37}$$

The diagonal entries in the inductance and capacitance matrices of a circuit represent the self-inductance and self-capacitance to ground of the circuit. The off-diagonal entries represent the mutual inductance and mutual capacitance.

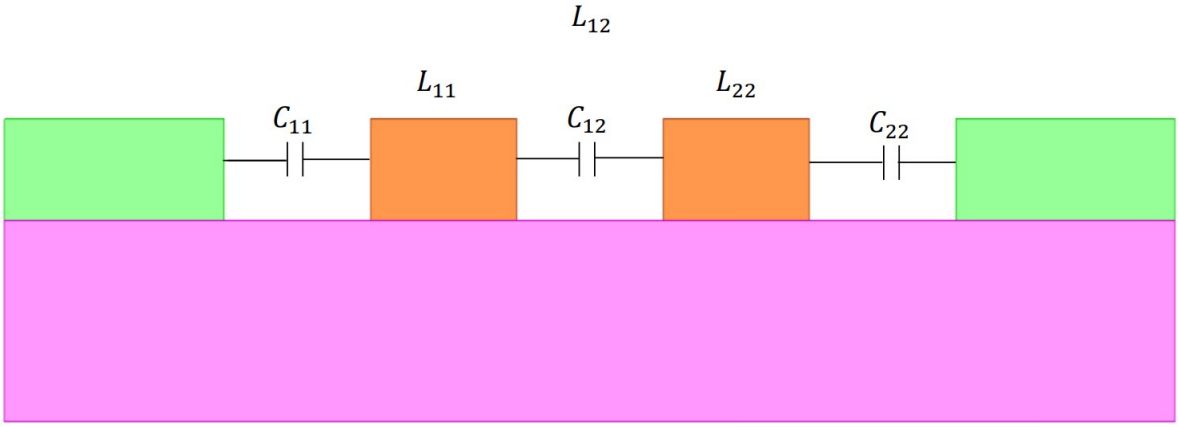

Figure 2.12: The cross section of a CCPW resonator, corresponding to Figure 2.11.

The differential mode of a resonator is characterized by applying the input signal differentially across the two center pins of the resonator. In this mode, the resonance frequency can be calculated using the following equation:

$$f_{diff} = \frac{1}{kl} \frac{1}{\sqrt{(L_{11} - |L_{12}|)(C_{11} + 2|C_{12}|)}} n, \tag{2.38}$$

The variable k represents the type of resonator being used. If the resonator is a half-wavelength resonator, then $k = 2$. Otherwise, $k = 4$. The variable l represents the physical length of the resonator, and $n \in \mathbb{N}$ represents the harmonic order.

In the common mode of a resonator, the applied signals have the same polarization. In this mode, the resonance frequency can be calculated using the following equation:

$$f_{comm} = \frac{1}{kl} \frac{1}{\sqrt{(L_{11} + |L_{12}|)(C_{11} - 2|C_{12}|)}} n. \tag{2.39}$$

2.7 Coupling

In electronics, coupling refers to transferring energy or signals between two or more components in a system. In electrical circuits, the coupling can occur in different ways depending on the physical arrangement of the components.

One common type of coupling is inductive coupling, which happens when two circuits share a common magnetic field. This type of coupling occurs when two coils are placed near each other and share a magnetic field. The magnetic field induces a current in the second coil, resulting in a transfer of energy or signals between the coils.

Another type of coupling is capacitive coupling, which occurs when two circuits share a common electric field across a capacitor. This type of coupling occurs when two conductive elements are separated by an insulating layer, forming a capacitor. The voltage on one element induces a voltage on the othert, leading to a transfer of energy or signals between the circuits. The strength of the capacitive coupling depends on the distance between the conductive elements and the dielectric properties of the insulating layer.

2.8 S-parameters

S-parameters describe the relationship between the incident and reflected electromagnetic waves at the ports of a network. They are represented as a matrix of complex values, and each S-parameter represents the ratio of the amplitude and phase of a reflected or transmitted wave to the amplitude and phase of an incident wave at a specific frequency. In other words, S-parameters provide a measure of how much energy is transmitted versus how much is reflected at each port of the network. They are commonly used in microwave engineering to analyze and design circuits, antennas, and other electromagnetic components.

If there is an incident wave of voltage V_1^+ from PORT 1 and we measure the reflected wave amplitude V_2^- at PORT 2, the S-parameter is $S_{21} = \frac{V_2^-}{V_1^+}$.[1] For an N-port network, the S-parameter is determined by,

$$S_{ij} = \frac{V_i^-}{V_j^+}, \quad i, j \in \mathbb{N}. \tag{2.40}$$

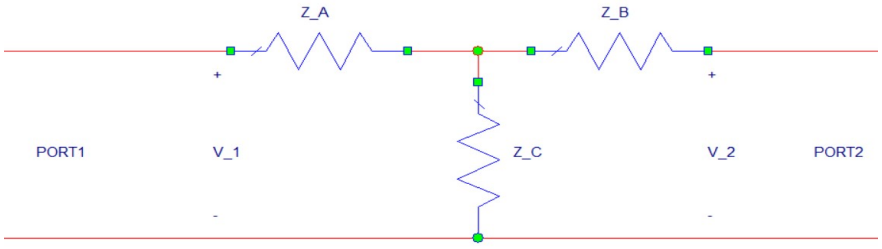

Figure 2.13: A two-port network.

When measuring the S-parameters of circuits, the output can be plotted as shown in Figure 2.14. Depending on the way the two ports are connected, the S-parameters will result in either a peak or a dip. The y-axis in the plot corresponds to equation (2.40) and indicates a significant change in the received signal. When measuring the S-parameters of a resonator circuit, the peak or dip frequency is considered to be the resonance frequency. In the case of a peak, the Δf_{-3dB} is the difference between the two frequencies that 3 dB lower than the peak frequency. For the dip case, the Δf_{-3dB} is the difference between the two frequencies at -3 dB.

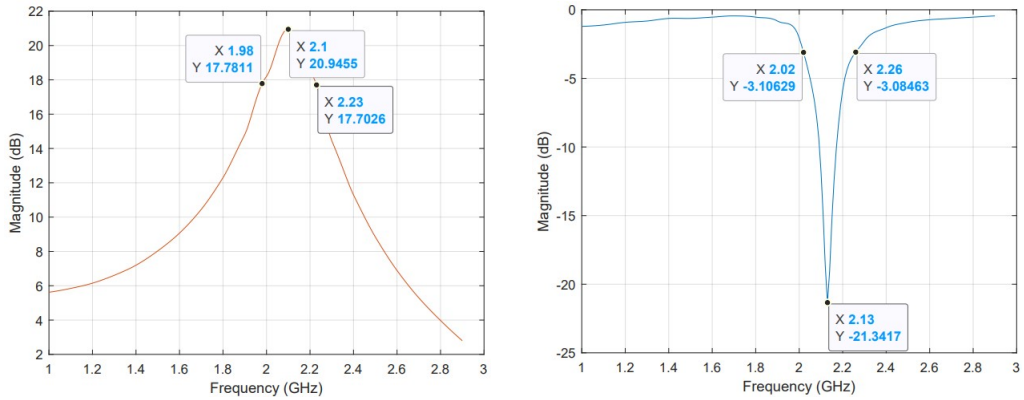

Figure 2.14: The magnitude of measured S-parameters in dB. Left: The peak sample resulted from the measurement. Right: The dip sample resulted from the measurement.

Chapter 3

Design & simulation

3.1 Goals

The main objective of the design is to achieve a specific quality factor for the resonator. The achievement is accomplished by implementing a transmission line, as depicted in Figure 3.1, through which signals are transmitted in and out. The resonator can selectively receive signals at the resonance frequency through coupling while filtering out others. The operating range of the high electron mobility transistor (HEMT) in our lab experimental setup sets a limit on the resonance frequency, which falls between 4 GHz and 8 GHz.

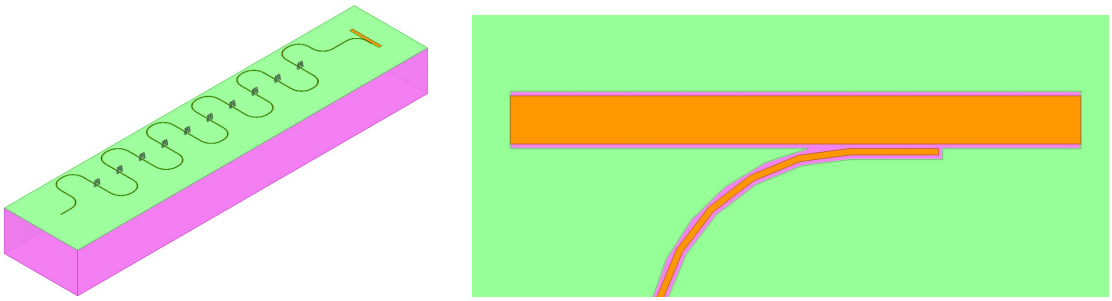

Figure 3.1: A quarter-wavelength resonator coupled to a transmission line. Left: The sinuous line is the resonator. The short straight line is the transmission line. Right: The coupling region of the transmission line and the resonator. The top straight line is the transmission line and its ends will connect to ports in a complete design.

In the context of this design, coupling refers to the energy exchange between the resonator and the transmission line, as demonstrated in Figure 3.2. This exchange is represented by a capacitor. A resonator is a device that stores energy in the form of oscillations at a specific frequency, and the coupling between the resonator and the transmission line enables energy transfer between them. The strength of this coupling determines the external quality

factor. The degree of coupling is usually regulated by adjusting the distance between the devices or altering the characteristics of the connecting material.

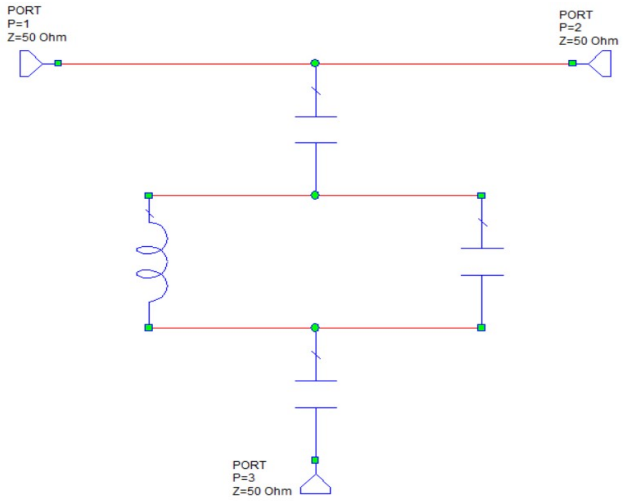

Figure 3.2: The diagram illustrates the connection between a resonator and a transmission line, with two ports designated as 1 and 2 at each end of the line. The resonator is modeled as an LC circuit, which has been simplified for ease of representation. This setup enables a coupling between the resonator and the transmission line that is analogous to that of a capacitor.

In the specific project described in the thesis, the other end of the resonator is left unloaded, as depicted in Figure 3.2. However, depending on the application requirements, it could also couple to a load.

Once the resonator system is designed, the main goal is to verify its resonance frequency and quality factor. The verification can be achieved by measuring the S-parameters, which can be obtained from Ports 1, 2, and 3 of the circuit.[10] Specifically, the input signal is fed through Port 1 and transferred to Port 2. At frequencies other than the resonance frequency, the signal will not couple with the resonator, whereas at the resonance frequency, the energy in the transmission line will be transferred to the resonator due to coupling. This results in the characteristic dip and peak observed in Figure 3.3, which confirms the resonance frequency and quality factor of the resonator.

In the project described below, the goal is to measure the material loss of quartz. Therefore, using equation (2.35), the quality factors obtained from both simulation and experiment can be utilized to calculate the intrinsic quality factor of quartz, which is a measure of its loss properties. The inverse of the internal quality factor is the loss tangent,

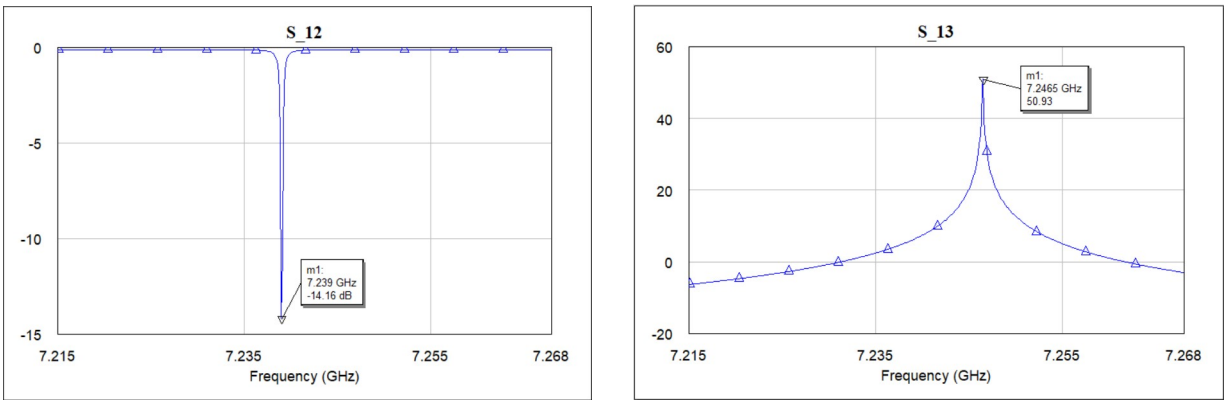

Figure 3.3: Ideal S-parameter results for the circuit in Figure 3.2. Left: The result measured from Port 1 and 2. Right: The result measured from Port 1 and 3.

which is a measure of the dissipation of energy in a dielectric material.[11] The loss tangent is defined as the tangent of the angle between the real and imaginary components of the complex permittivity of the material.

3.2 Design

The project aims to measure the material loss of ST-cut crystalline quartz in Figure 3.4. Material loss refers to the energy or power dissipation within a material due to its electrical conductivity.[12] This loss can be determined by measuring the quality factor of the quartz resonator. To do so, a circuit is designed with a resonator placed on the quartz substrate, and the internal quality factor, Q_r, is replaced by the quartz's loss as the equation (2.35). The circuit's external quality factor, Q_e, measures the coupling quality between the transmission line and the resonator. To determine the material loss of the quartz, the coupling quality factor is controlled during circuit design. During the experimental phase, the chip containing the quartz substrate with the controlled Q_e is placed in a dilution fridge, decreasing the temperature to 10 mK to create a lossless environment. The quality factor Q of the resonator can be measured and analyzed to extract Q_r, to evaluate the material loss of the quartz.

The circuit in this project is fabricated using aluminum, which is a superconducting material at temperatures below 1.2 K.[14] Consequently, when the chip is cooled to this temperature in the fridge, there is negligible extra loss due to metal resistance. This property

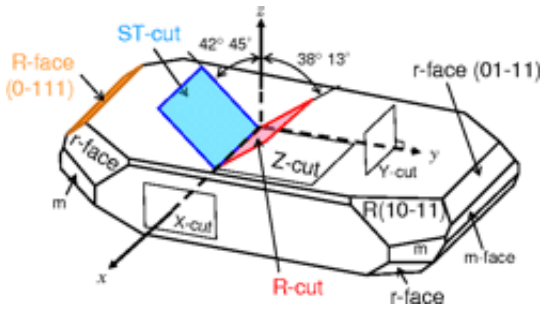

Figure 3.4: The different cuts on a quartz substrate.[13]

of aluminum is advantageous in the sense that it minimizes the loss in the resonator and enhances the sensitivity of the measurements.

The design process commences with a transmission line comprising two 50 Ω ports. Since all other electrical components in the experiment are also 50 Ω, the ports are deliberately configured as 50 Ω to prevent any impedance mismatch. In addition, the transmission line's impedance is also set to 50 Ω to further prevent any mismatch. To streamline the fabrication process, a CPW resonator is utilized to couple to the transmission line. This resonator also has an impedance of 50 Ω as a matter of design standard.

To optimize the use of equation (2.35) for circuit design, we have made predictions for the quality factor of quartz at 5×10^3, 5×10^4, and 5×10^5. Additionally, since the experiment conditions necessitate measurements between 4 and 8 GHz, we have designed three groups of resonators, each with a different quality factor. Within each group, there are eight resonators with frequencies that vary from 4 to 8 GHz, as illustrated in Figure 3.5. Since the resonators only couple to the transmission line at their respective frequencies, multiple resonators coupled to the same transmission line will not affect each resonator's behavior.

	transmission line	resonator
conductor width (μm)	22	3
gap width (μm)	2	2

Table 3.1: The widths of the designed transmission lines and resonators.

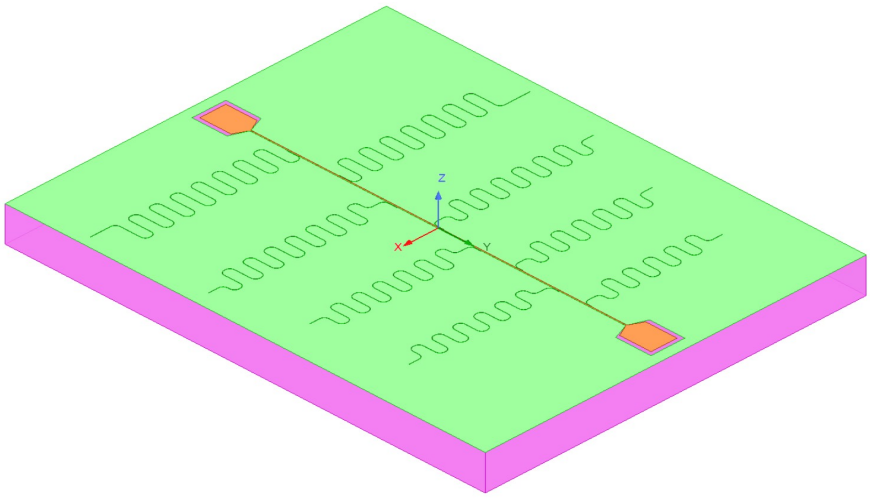

Figure 3.5: The complete design includes a purple quartz substrate, with a green section representing the ground and an orange section describing the transmission line. Additionally, the winding lines represent the resonator.

3.3 Simulation

The circuit design was implemented in Python using the Qiskit Metal environment, and the resulting resonators and transmission lines were uploaded into Ansys. Within the software, we employed the eigenmode solution type to obtain a preliminary estimate of the resonator frequency. This solution type simulates all the resonances in the model and allows us to analyze the resonance frequency of each resonator individually, as demonstrated in Figure 3.1.

The software utilizes the finite-element method to solve Maxwell's equations that govern electromagnetic fields. This approach primarily involves meshing, whereby the software divides the circuit design into several geometries known as mesh cells. Each mesh cell has a uniform electric field strength. The software employs mesh cells to predict the electrical field in real-life measurements. After each simulation pass, the software reduces the sizes of the cells. As a result, the outcomes derived from different mesh cells are distinct. To compute the change in frequency, each result is compared with the previous one to come up to the Max Delta Frequency in percentage, in Figure 3.6. The simulation runs until the change converges to the target value of the Maximum Delta Frequency Per Pass. The simulation ends when the Delta function meets the target, unless the Minimum Number of Passes and Minimum Converged Pass in Setup are assigned with other values other than 1.

After running the simulation, the eigenmode data obtained from the results should be close to the frequency of the designed resonator. Moreover, the simulated design must match the expected configuration before simulations to ensure the frequency's reliability. Additionally, as shown in Figure 3.6, the solutions should converge with the change in frequencies reaching the target set in the setup. The target cannot be zero, as the solutions would take infinite time to converge under such conditions. Other critical factors need to verify include the meshing and electrical field. The meshing cells should be smaller inside the resonator than on the ground, and the electrical field should be stronger around the resonator than in other regions because the resonator is resonating, and energy is transferred from the transmission line to the resonator. As demonstrated in Figure 3.6, the red dots around the resonator signify that energy is successfully transferred to the resonator.

Figure 3.6 represents the energy stored in the resonator as the magnitude of the electrical field. In this figure, the resonator is a $\frac{\lambda}{4}$ resonator. As shown in Figure 2.9, the magnitude of the electrical field should be strong at one end and close to zero at the other end. This change in the field can be utilized to verify the proper design of the resonator. For a $\frac{\lambda}{2}$ resonator with both ends shorted, the field is close to zero at both ends. Conversely, for a resonator with both ends open, the field is strong at both ends.

Eigenmode simulations are used to obtain a rough resonator frequency, which is then used to specify the subsequent simulation. Since the eigenmode simulation is not intended to provide highly accurate results, the setup does not need to be very refined, and as a result, the simulation time is relatively short. After obtaining the rough resonator frequency, the design is then changed to the HFSS (High-Frequency Structure Simulator) solution type. The HFSS simulation can produce an S-parameter plot, which is helpful for accurately determining the resonator frequencies and coupling quality factors.

The HFSS simulation uses the same design as the previous simulation but adds two 50 Ω ports at the ends of the transmission line. An integration line is defined on the ports from the ground to the ends of the transmission line to show the signal's path. The rough frequency obtained from the previous eigenmode simulation is the default frequency in the HFSS solution setup. Using the defaulty frequency ensures that the simulation does not diverge and is less likely to encounter errors.

When simulation parameters such as mesh cell size, number of passes, or other settings are not correctly defined, the simulation can fail, as shown in Figure 3.7. In comparison to

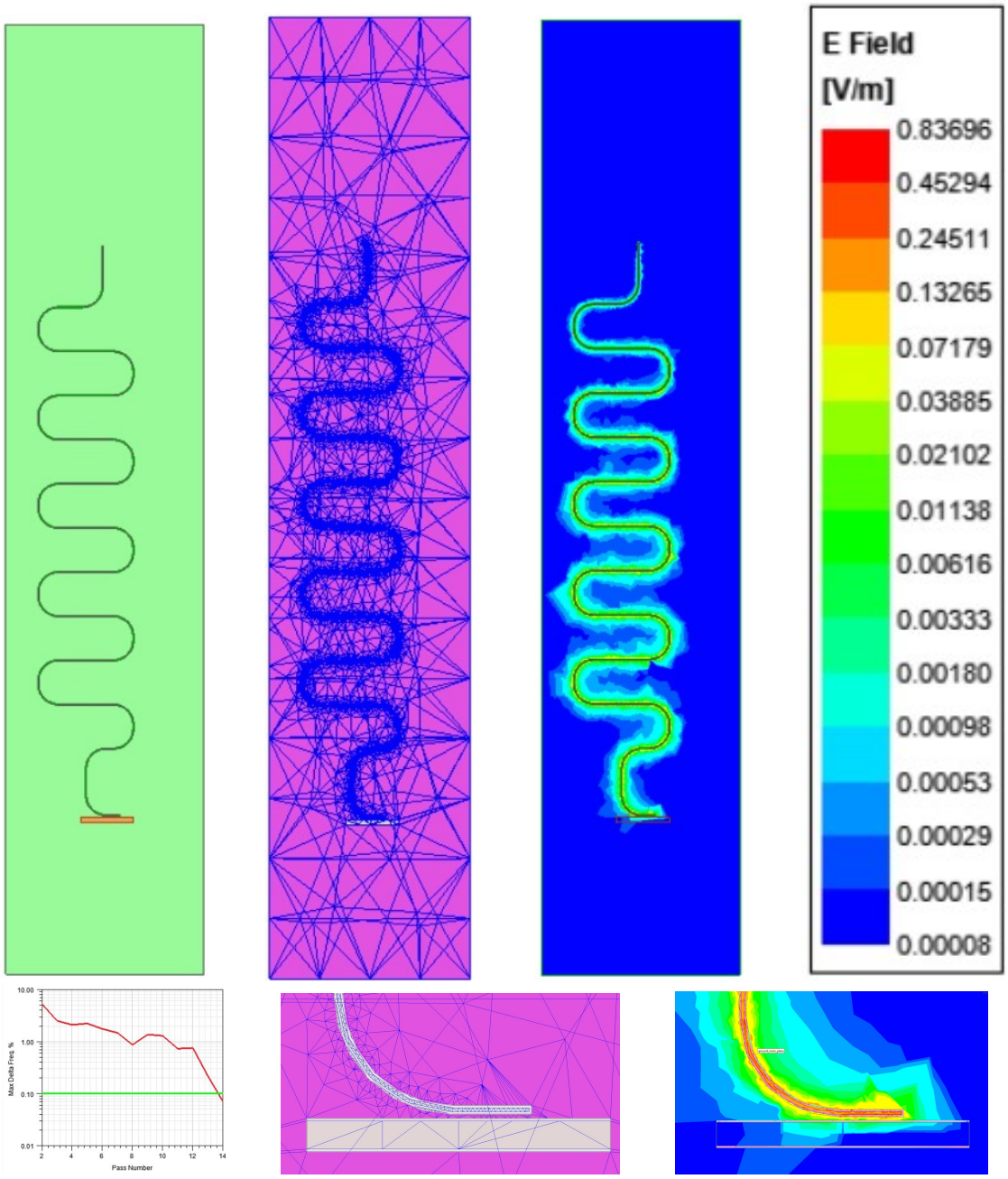

Figure 3.6: The eigenmode simulations were performed on a resonator with a frequency of 4.75 GHz. The results are presented from left to right: (a) The resonator is designed to couple to a piece of a transmission line. (b) The mesh cells were generated after the simulation. (c) The magnitude of the electrical field is represented on a logarithmic scale. (d) The legend of the electrical field. (e) The Max Delta Frequency (%) versus Pass Number. The green line indicates the target set, while the red line represents the difference after each pass. The simulation continued until the change in frequency converged to the set target value. (f) The meshing in the coupling region. (g) The electrical field near the resonator in the coupling region.

the figures in Figure 3.6, in the electrical plot in Figure 3.7, energy from the transmission line is not transferred to the resonator. Additionally, in the mesh plot in Figure 3.7, the mesh cells are too large to show an accurate change in the electrical field of the design. To solve the issues, we can adjust the cells' sizes smaller and assign a larger value for the Minimum Converged Passes compared with the last failed setup. Meanwhile, check if the Frequency in HFSS setup equals to the result from the eigenmode to avoid divergence.

Once all parameter issues have been resolved, an S-parameter plot can be generated, as shown in the last plot in Figure 3.8. From this plot, the resonance frequency and coupling quality factor can be easily determined.

Resonators can be modeled as LC circuits, and their frequencies can be calculated using equations (2.24) and (2.32). ANSYS 2D Extractor provides a way to simulate the inductance and capacitance of resonators. This tool uses finite element analysis to solve for the electric and magnetic fields within the resonator, taking into account the material properties and boundary conditions. Using these fields, ANSYS 2D Extractor calculates various properties of interest, including capacitance and inductance. However, this tool only works for 2D designs, such as the cross-section of a resonator shown in Figure 3.9. The tool calculates the capacitance and inductance L_{11}, L_{12}, C_{11}, and C_{12} with respect to Figure 2.11. With these values, equation (2.37) and (2.38 can be used to calculate the resonator frequency. Based on the equation, the total length of the resonator is required to apply to determine the resonance frequency.

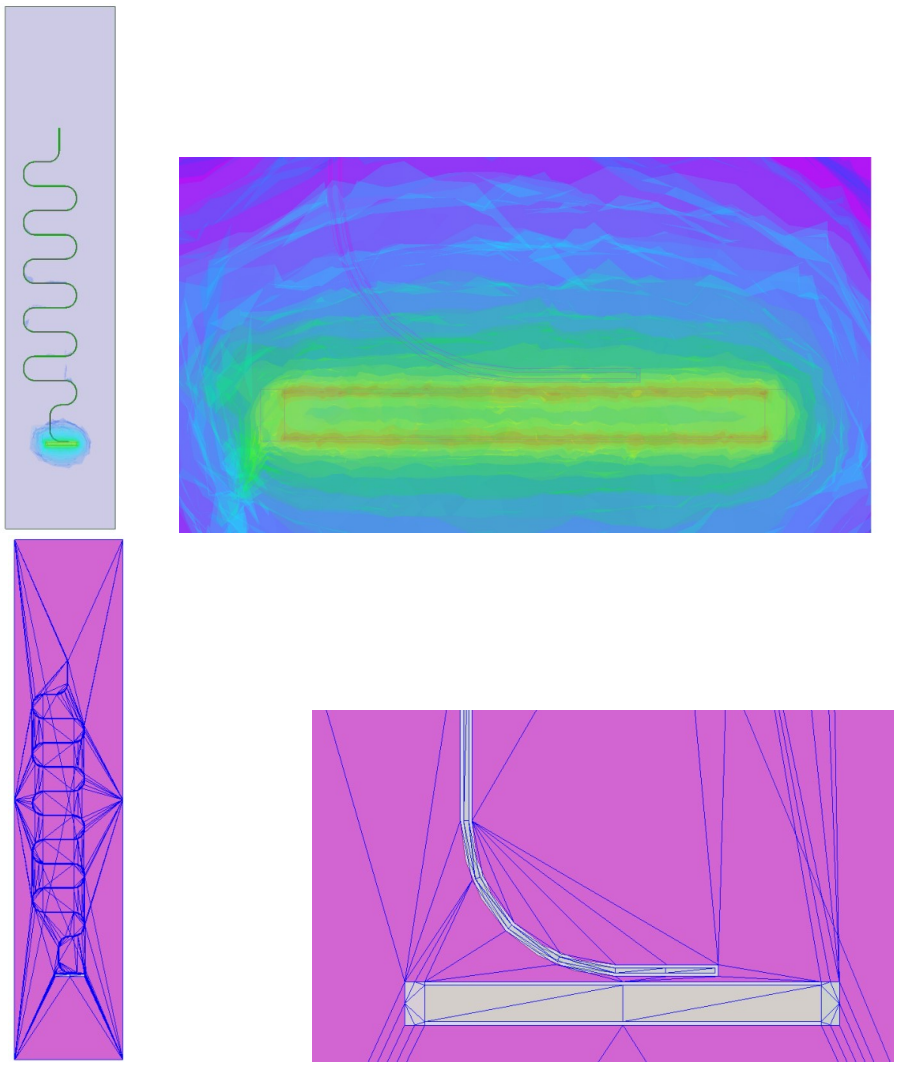

Figure 3.7: The HFSS simulations of the resonator. From left to right: (a) The failed simulation's magnitude electrical field in log scale. (b) The detail of (a) at the coupling region. (c) The failed simulation's meshing. (d) The detail of (c) at the coupling region.

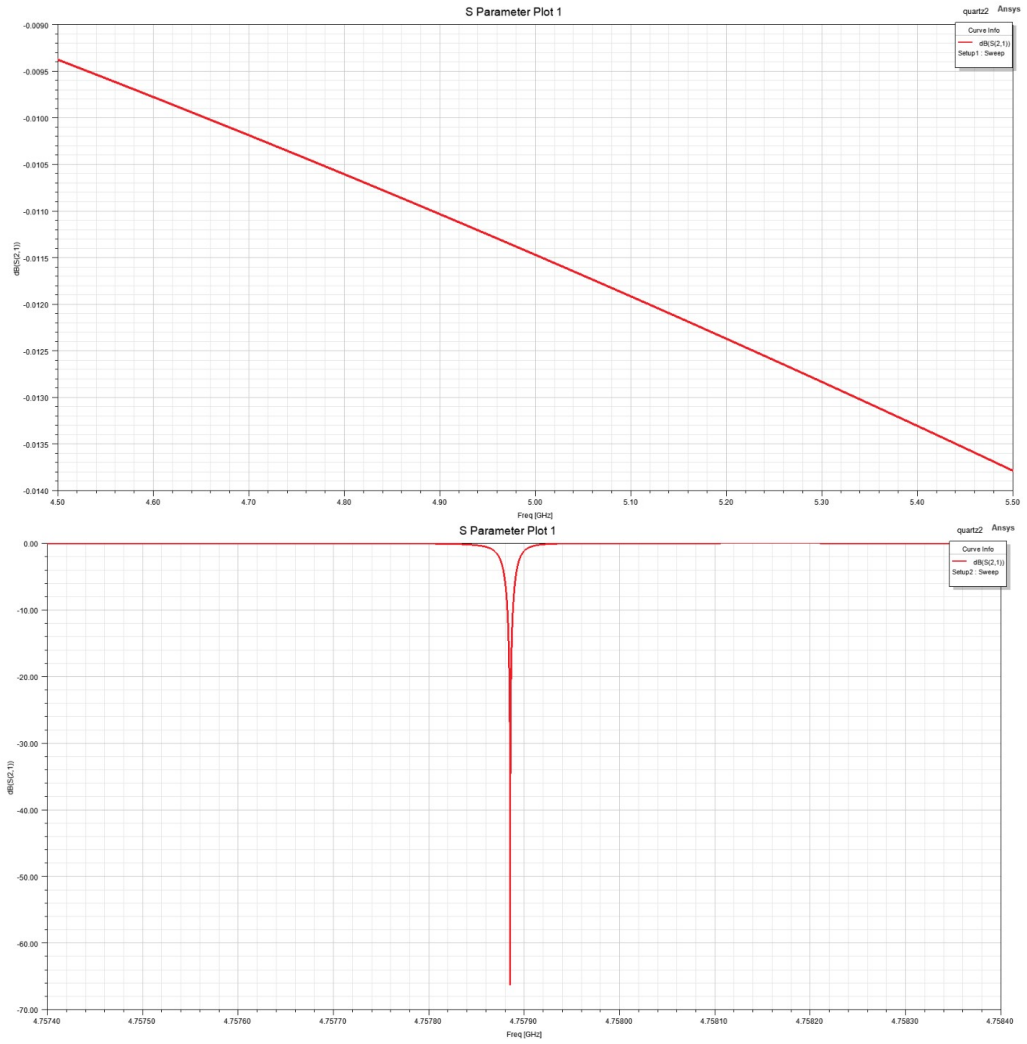

Figure 3.8: The HFSS simulations of the resonator. Upper: The failed simulation's S-parameter plot. Lower: The successful simulation's S-parameter plot.

Figure 3.9: The cross-section of a CPW resonator. The yellow part is the substrate. The blue part is the ground. The red part is the center pin.

Chapter 4

Other applications

Designing superconducting CPW resonators is a fundamental task in the field of superconducting electronics. However, while these resonators can provide valuable information about material properties and device performance, they are not immune to fabrication issues and other sources of noise that can affect their performance. By exploring different kinds of resonators, such as transmission line resonators and CCPW resonators, we can develop a more comprehensive understanding of the fabrication process and how it impacts device performance. Additionally, by applying kinetic inductance to tune the frequency of these resonators, we can further optimize their performance and develop more sensitive and accurate detectors. This approach has the potential to enhance the capabilities of superconducting electronics and enable the development of new technologies with a wide range of applications.

4.1 Fabrication issue detection

The resonator designs are typically fabricated on silicon wafer, but inaccuracies in the lithography and etching processes can result in changes to the resonator structures. These changes can cause the estimated resonance frequencies to deviate from the designed frequencies, indicating the need to modify the designs.

Lithography transfers patterns onto the substrate and issues with this process can be detected using an environmental scanning electron microscope. However, issues caused by the etching process are more difficult to detect. The chips containing the resonator designs are expected to be fabricated with superconducting materials deposited on the silicon substrate. To create the design, regions of the superconductor layer need to be removed through etching.

Ideally, the superconductor layer is etched evenly, as shown in Figure 4.1. However, when using niobium as the superconductor layer with dry etching, it can be challenging to control the process, resulting in over-etching, as shown in Figure 4.2. The trench depth created by over-etching can change the resonator geometry, which is directly related to the resonator frequency. ANSYS simulations have shown that this issue can result in a frequency shift of more than 1 GHz from the original design. To address the problem, the layer has been changed to aluminum, and wet etching is used instead of dry etching.

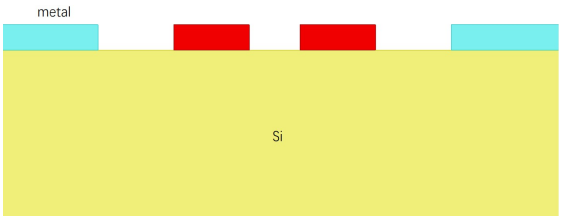

Figure 4.1: The cross-section of a CCPW resonator from an ideal etching result. The etching process takes off all the metal in the trench area and doesn't etch the substrate.

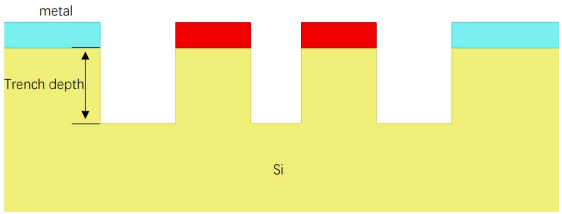

Figure 4.2: The cross-section of a CCPW resonator from an over-etch made by niobium layer with dry etch receipt.

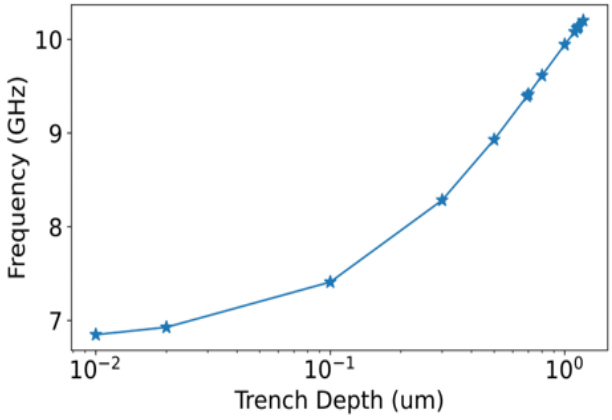

Figure 4.3: The resonator frequency v.s. Trench depth.

In addition to potential etching issues, the well-developed chip has the capacity for other applications on the resonator. Specifically, we have explored the use of Neon in this

context. However, determining the appropriate distribution for depositing the Neon onto the circuit has proved to be a significant challenge. Due to the neon's freezing point of 24.56 K, the deposition process can only be performed inside a dilution fridge.[15] Consequently, the process cannot be observed directly since the fridge is opaque. Figure 4.4 displays the fridge setup, with the dim blue region representing the inside of the fridge and the brown sample package where the chips will be placed. It's crucial to note that measuring techniques like laser interferometry may disrupt the limited cooling power of the fridge, which stands at about 100 μW. Additionally, because the dielectric constant of neon differs from that of a vacuum, the inductance and capacitance shown in Figure 2.12 change. So, the resonance frequencies measured with and without neon will vary. This difference may suggest the distribution of neon on the chip, as demonstrated in the plot in Figure 4.6.

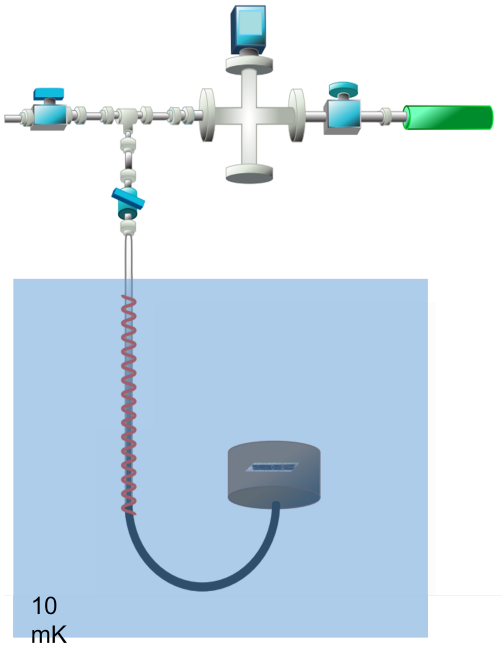

Figure 4.4: The experimental setup of the dilution fridge and how to place the chip. The green cylinder is the Neon container. The other objects outside the dim blue region are the valves and gauges. The dim blue region demotes the inside setup of a dilution fridge.

The predicted structure for Neon deposition is depicted in Figure 4.5. As illustrated, the Neon covers only a portion of the resonator, leading to a change in the resonance frequency solely in the covered area. The remaining sections of the resonator maintain their original frequency. Consequently, the total frequency of the resonator is a combination of the two

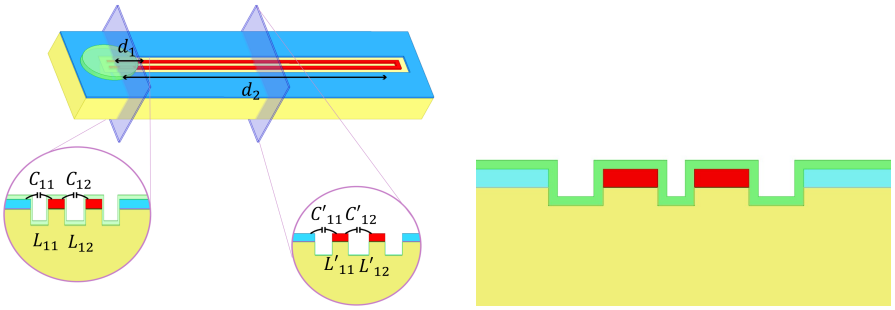

Figure 4.5: The neon deposition on a resonator. Left: The neon deposition on the resonator and the cross sections with and without neon covering. Right: The cross-section of the resonator with neon deposited.

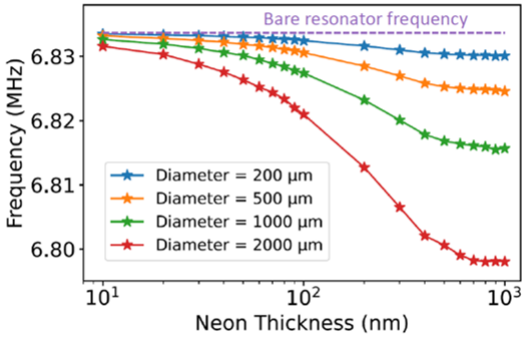

Figure 4.6: The frequency shift v.s. the neon thickness change. The diameter is $2d_1$ in Figure 4.5.

parts, and it can be calculated using Equation (2.38) and the distances between the resonator with and without Neon.[16]

$$f = \frac{1}{8\pi d_1\sqrt{(L_{11}-|L_{12}|)(C_{11}+2|C_{12}|)}+8\pi(d_2-d_1)\sqrt{(L'_{11}-|L'_{12}|)(C'_{11}+2|C'_{12}|)}} \tag{4.1}$$

The frequency equation is employed in the context of a differential mode resonator, which is designed with varying voltage applied to its center pins. This specific design allows the resonator to attract electrons, effectively mitigating their presence above the neon layer. As a result, we can successfully trap these electrons and utilize them as quantum bits.

By utilizing the capacitance and inductance values obtained from ANSYS 2D Extractor simulation along with the specified neon deposition radius, generating the plot in Figure

4.6 is a straightforward process. Thus, measuring the resonator frequencies both before and after the deposition of neon allows for determining the distribution of neon on the chip.

4.2 Resonator frequency tuning

When direct current (DC) is applied to a resonator, it can alter the resonator's frequency.[17] Since a resonator functions as an LC circuit, any change in capacitance or inductance results in a corresponding change in frequency. In most circuits, the inductance is mainly based on the magnetic field generated by a straight wire or coil, which depends on the energy stored in the field due to the current flowing through it. But the kinetic inductance arises from the kinetic energy stored in the motion of the charge carriers. The kinetic inductance will be observed in superconductor at high frequency. At low frequency, the motion will be counteracted and the kinetic inductance becomes negligible.

When a conductor is subjected to an alternating electric field, the mobile charge carriers in the conductor, such as electrons, experience a force due to their inertia, similar to the way a moving object resists changes to its motion.[18] This results in an equivalent series inductance, which is a measure of the conductor's opposition to changes in current. In other words, the conductor behaves like an inductor due to the motion of the mobile charge carriers, which gives rise to the concept of kinetic inductance. Therefore, applying a DC source to the resonator tunes the resonance frequency.

The kinetic inductance depends on the charge carrier density n,

$$L_K = \frac{m_e}{ne^2}\frac{l}{A}. \tag{4.2}$$

In the given context, m_e represents the electron mass, n corresponds to the charge carrier density, l denotes the length of the conductor, and A represents the cross-sectional area of the conductor. Considering that the center pin of the resonator functions as a conductor for applying the DC source, we can regard l and A as measurements specific to the center pin.

However, connecting the DC source directly to the resonator is not feasible, as it requires the two ends of the resonator to be connected to two wire-bonding pads. This method changes

the center pin length of the resonator due to the geometry of a CPW resonator, as shown in Figure 2.9, which affects the resonator's designed properties.

We incorporate two identical third-order low-pass Butterworth filters to mitigate this effect between the $\frac{\lambda}{2}$ resonator ends and the pads. These filters can filter out any noise sources other than the DC source while also preventing energy leakage from the resonator from maintaining its coupling quality factor.[19] The Butterworth filter is designed to achieve a flat passband and is composed of two capacitors and one inductor to optimize its size.

	inductance (nH)	capacitance 1 (pF)	capacitance 2 (pF)	cutoff frequency (GHz)	S-parameter at 4GHz
1	55.9	1.99	1.99	0.333	-40.0
2	16.0	4.55	4.55	0.881	-42.3
3	10.6	6.00	6.00	0.973	-43.4

Table 4.1: The design of an ideal discrete Butterworth filter has been optimized for size using both inductance and capacitance components.

In a discrete circuit, the ideal filter looks like the one shown in Figure 4.7. To allow only the DC source to pass, the cutoff frequency at -3 dB should be as low as possible while maintaining an S-parameter at the resonator measurement's lower band of less than -36 dB to preserve the quality factor of the resonator above 10^4. However, in an integrated filter, parasitic capacitances exist between the inductor and the ground, and between each wire of the inductor, which can create self-resonance, as shown in Figure 4.8. Increasing the spacing between the inductor and the ground and between each wire can reduce the effect of the parasitic capacitances, but some self-resonance will remain.

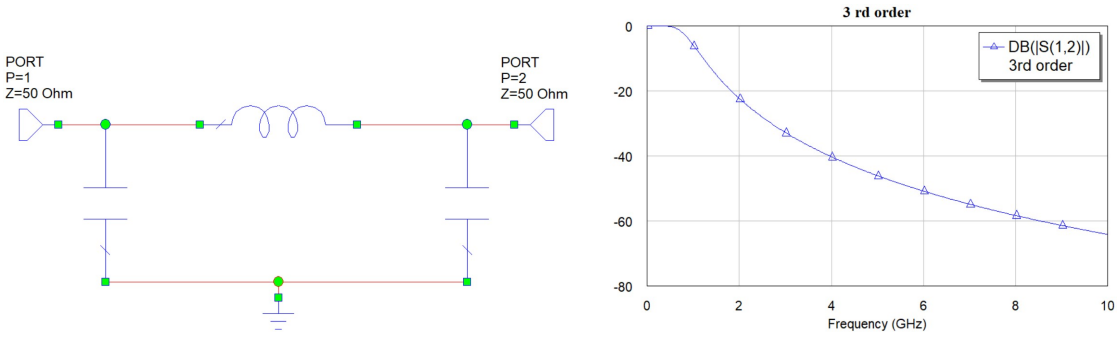

Figure 4.7: The equivalent discrete circuit for an ideal third-order low-pass filter, with its S-parameter plot.

The integrated filter's components do not follow a π-structure. Instead, the design shown in Figure 4.9 was implemented to maintain electrons within the circuit and prevent energy

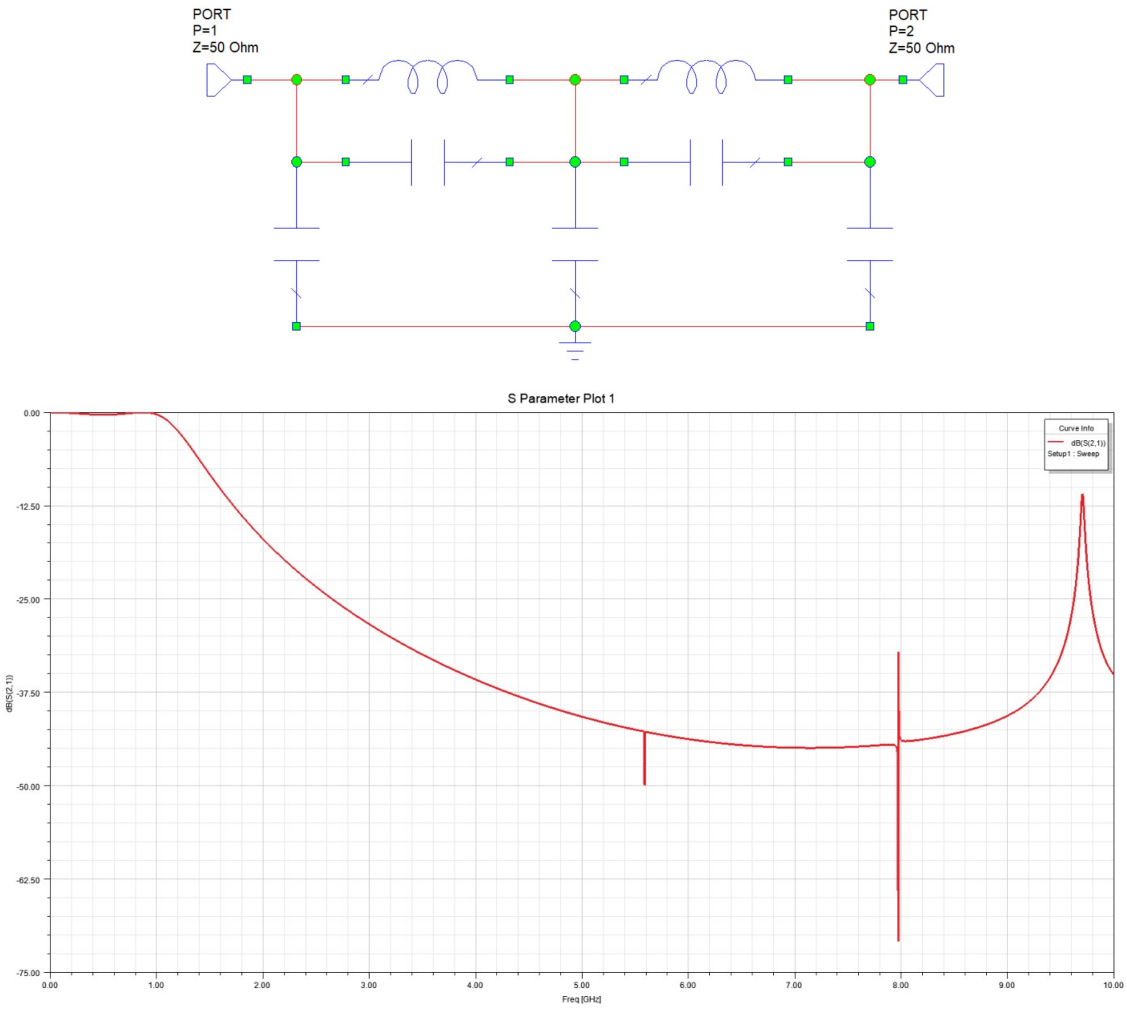

Figure 4.8: The equivalent discrete circuit for an integrated filter, with its S-parameter plot.

leakage. In the coupling region, the transmission line is coupled to the half-wavelength CPW resonator, reducing any extraneous coupling to the resonator while also accommodating the sample package's feedline design. The ports at the transmission line's ends enable signal transfer, while the pads at the ends of the filters serve as a DC source. The S-parameters exhibit similar characteristics to those shown in Figure 3.6(f), with variations in frequency and quality factor. By applying the DC source to the resonator, the S-parameters measured from the transmission line's two ports can be used to monitor frequency changes.

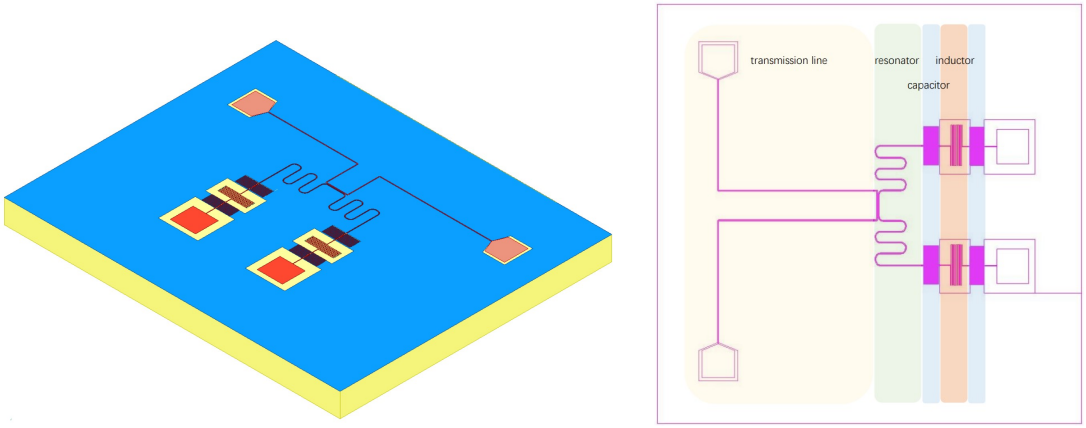

Figure 4.9: The entire design with resonator and filters, including the 3D view and the GDS file view.

Chapter 5

Conclusion

In conclusion, this thesis has investigated the design and characterization of microwave superconducting resonators for materials characterization. We have explored the transmission line theory, different kinds of resonators, coupling, quality factors, and S-parameters. Moreover, we have developed and demonstrated projects for characterizing quartz's material loss, detecting chip fabrication issues, developing tunable resonators, and demonstrating using electronic simulation software.

Our research has contributed significantly to the field of materials characterization, specifically in the area of microwave superconducting resonators. We have demonstrated that the resonators designed and developed in this thesis can be used for a wide range of applications in material science, including characterizing the dielectric properties of materials, detecting fabrication issues, and developing tunable resonators. Furthermore, our work has contributed to understanding the relationship between the resonator's design parameters and performance, which can guide future research in this area.

Although this thesis has some limitations, such as the need for further experimental validation and optimization of the resonators, our findings suggest the excellent potential for microwave superconducting resonators in materials characterization. In the future, it will be interesting to explore the use of these resonators in other areas of material science, such as the characterization of magnetic and superconducting materials.

In conclusion, this thesis provides a foundation for further research in microwave superconducting resonators for materials characterization. The findings of this research are expected to contribute to the development of more advanced and accurate techniques for characterizing materials, which will have significant implications for various industries, including electronics, healthcare, and renewable energy.

References

[1] D. M. Pozar, *Microwave Engineering*. John Wiley & Sons, Inc, fourth ed., 2012.

[2] W. C. Chew, *Lectures on Electromagnetic Field Theory*. 2021.

[3] A. M. Niknejad, *Electromagnetics for High-Speed Analog and Digital Communication Circuits*. Cambridge University Press, 2007.

[4] M. Schwartz, *Reflection, Transmission and Impedance*. Class Lecture, Waves, Lecture 9, Harvard University, 2016.

[5] S. V. I., *60 Years of Electrically Small Antennas Theory*. 2007.

[6] F. D. Paolo, *Networks and Devices Using Planar Transmissions Lines*. 2000.

[7] M. B. M. Göppl, A. Fragner, *Coplanar waveguide resonators for circuit quantum electrodynamics*. Journal of Applied Physics 104, 113904 https://doi.org/10.1063/1.3010859, 2008.

[8] R. M. L. Baez, *Coplanar stripline resonators for Andreev quantum bits*. Chalmers University of Technology, Gothenburg, Sweden, 2021.

[9] G. Koolstra, *Trapping a Single Electron on Superfluid Helium Using a Superconducting Resonator*. The University of Chicago, Department of Physics, 2019.

[10] D. S. Wisbey, *New method for determining the quality factor and resonance frequency of superconducting micro-resonators from sonnet simulations*. J Low Temp Phys 176, 538–544. https://doi.org/10.1007/s10909-014-1099-3, 2014.

[11] J. T. M. N. J. T. X. D. P. M. H. E. A. H. D. S. W. K. W. M. D. Kowsari, K. Zheng, *Fabrication and surface treatment of electron-beam evaporated niobium for low-loss coplanar waveguide resonators*, vol. 119 (13): 132601. https://doi.org/10.1063/5.0066441. Applied Physics Letter, 2021.

[12] C. R. H. McRae, *Materials loss measurements using superconducting microwave resonators*. Review of Scientific Instruments 91, 091101; https://doi.org/10.1063/5.0017378, 2020.

[13] S. Chiashi, H. Okabe, T. Inoue, J. Shiomi, T. Sato, S. Kono, M. Terasawa, and S. Maruyama, *Growth of Horizontally Aligned Single-Walled Carbon Nanotubes on the Singular R-Plane (10–11) of Quartz*, vol. 116. Journal of Physical Chemistry C, 2012.

[14] E. P. Harris, *Critical Field of Superconducting Aluminum as A Function of Temperature and Pressure above 0.3 K*. 1966.

[15] K. G. Z. X. Zhou, X., *Single electrons on solid neon as a solid-state qubit platform*. Nature 605, 46–50. https://doi.org/10.1038/s41586-022-04539-x, 2022.

[16] G. Koolstra, *Trapping a single electron on superfluid helium using a superconducting resonator*. University of Chicago https://doi.org/10.6082/uchicago.2070, 2019.

[17] A. J. Annunziata, *Tunable superconducting nanoinductors*. Nanotechnology 21 445202 10.1088/0957-4484/21/44/445202, 2010.

[18] R. Meservey and P. M. Tedrow, *Measurements of the Kinetic Inductance of Superconducting Linear Structures*, vol. 40 (5). Journal of Applied Physical, 1969.

[19] S.-X. Li and J. B. Kycia, *Applying a Direct Current Bias to Superconducting Microwave Resonators by Using superconducting Quarter Wavelength Band Stop Filter*. Appl. Phys. Lett. 102, 242601 https://doi.org/10.1063/1.4808364, 2013.